



1 **The impact of multi-species surface chemical observations**
2 **assimilation on the air quality forecasts in China**

3 Zhen Peng^{1*}, Lili Lei¹, Zhiqian Liu^{2*}, Jianning Sun^{1,3}, Aijun Ding^{1,3}, Junmei Ban²,
4 Dan Chen⁴, Xingxia Kou⁴, Kekuan Chu¹

5 1 School of Atmospheric Sciences, Nanjing University, Nanjing, China

6 2 National Center for Atmospheric Research, Boulder, Colorado, USA

7 3 Institute for Climate and Global Change Research, Nanjing University, Nanjing,
8 China

9 4 Institute of Urban Meteorology, CMA, Beijing, China

10

11 **Abstract.** An Ensemble Kalman Filter data assimilation (DA) system has been
12 developed to improve air quality forecasts using surface measurements of PM₁₀, PM_{2.5},
13 SO₂, NO₂, O₃ and CO together with an online regional chemical transport model, WRF-
14 Chem (Weather Research and Forecasting with Chemistry). This DA system was
15 applied to simultaneously adjust the chemical initial conditions (ICs) and emission
16 inputs of the species affecting PM₁₀, PM_{2.5}, SO₂, NO₂, O₃ and CO concentrations during
17 an extreme haze episode that occurred in early October 2014 over the East Asia.
18 Numerical experimental results indicate that ICs play key roles in PM_{2.5}, PM₁₀ and CO
19 forecasts during the severe haze episode over the North China Plain. The 72-h
20 verification forecasts with the optimized ICs and emissions performed very similarly to
21 the verification forecasts with only optimized ICs and the prescribed emissions. For the
22 first-day forecast, near perfect verification forecasts results were achieved. However,
23 with longer range forecasts, the DA impacts decayed quickly. For the SO₂ verification
24 forecasts, it was efficient to improve the SO₂ forecast via the joint adjustment of SO₂
25 ICs and emissions. Large improvements were achieved for SO₂ forecasts with both the
26 optimized ICs and emissions for the whole 72-h forecast range. Similar improvements
27 were achieved for SO₂ forecasts with optimized ICs only for just the first 3 h, and then
28 the impact of the ICs decayed quickly. For the NO₂ verification forecasts, both forecasts
29 performed much worse than the control run without DA. Plus, the 72-h O₃ verification



30 forecasts performed worse than the control run during the daytime, due to the worse
31 performance of the NO₂ forecasts, even though they performed better at night. However,
32 relatively favorable NO₂ and O₃ forecast results were achieved for the Yangtze River
33 delta and Pearl River delta regions.

34

35 **1 Introduction**

36 Predicting and simulating air quality remains a challenge in heavily polluted regions
37 (Wang et al., 2014; Ding et al. 2016). Chemical data assimilation (DA), which
38 combines observations and model simulations, is recognized as one effective method
39 to improve air quality forecasts. It has been widely used to assimilate aerosol
40 measurements from both ground-based and space-borne platforms, including surface
41 PM₁₀ observations (Jiang et al., 2013; Pagowski et al., 2014), surface PM_{2.5}
42 observations (Li et al., 2013; Zhang, 2016), Lidar observations (Yumimoto et al., 2007,
43 2008), aerosol optical depth products from AERONET (the AErosol RObotic
44 NETwork) (Schutgens et al., 2010a-b, 2012), and from various satellites (Sekiyama et
45 al., 2010; Liu et al., 2011; Dai et al., 2014). These studies indicate that assimilating
46 observations can substantially improve the spatiotemporal variations of aerosol in the
47 simulation and forecasts.

48 Aerosols are not only primarily emitted, but also with a larger portion secondary
49 formed through reactions with several gaseous-phases precursors and oxidants in the
50 atmosphere (Huang et al., 2014; Nie et al., 2014; Xie et al., 2015). So, observations of
51 trace gases are also useful in assimilating data for aerosol simulations and forecasts.
52 Efforts to assimilate atmospheric-composition observations, like O₃, SO₂, NO, NO₂,
53 CO, and NH₃, have also been made. For example, Elbern et al. (1997, 1999, 2000, 2001,
54 2007) developed a 4D-VAR (four-dimensional variational) system to assimilate surface
55 measurements of O₃, SO₂, NO and NO₂ to improve air quality forecasts with the joint
56 adjustment of initial conditions (ICs) and emission rates. Later, van Loon et al. (2000)
57 assimilated O₃ in the transport chemistry model LOTOS, based on an Ensemble Kalman
58 Filter (EnKF). Heemink and Segers (2002) attempted to reconstruct NO_x and volatile
59 organic compound (VOC) emissions for O₃ forecasting by assimilating O₃. Carmichael



60 et al. (2003, 2008a, 2008b) developed 4D-VAR and EnKF systems to assimilate O₃ and
61 NO₂ to improve ICs and emission sources for O₃ forecasting. Hakami et al. (2005)
62 constrained black carbon (BC) emissions during the Asian Pacific Regional Aerosol
63 Characterization Experiment. Henze et al. (2007, 2009) estimated SO_x, NO_x and NH₃
64 emissions based on a 4D-VAR method by assimilating surface sulfate and nitrate
65 aerosol observations. Other studies have estimated the NO_x (van der et al., 2006, 2017;
66 Mijling et al., 2009, 2012, 2013; Ding, et al., 2015) and SO₂ emissions (van der et al.,
67 2017) based on an extended Kalman filter by assimilating SO₂ and NO₂ retrievals from
68 SCIAMACHY (SCanning Imaging Absorption spectroMeter for Atmospheric
69 CHartographY) and OMI (Ozone Monitoring Instrument). Barbu et al. (2009) applied
70 an EnKF to optimize the emissions and conversion rates using surface measurements
71 of SO₂ and sulfate. McLinden (2016) constrained SO₂ emissions using space-based
72 observations.

73 In recent years, severe haze pollution episodes have begun to occur more
74 frequently in China, especially in the megacity clusters of eastern China (e.g., Parrish
75 and Zhu, 2009; Sun et al., 2015; Zhang et al., 2015a). Thus, regional haze, especially
76 when accompanied by extremely high PM_{2.5} concentrations, has drawn significant
77 research interest. However, there are large uncertainties involved in the numerical
78 prediction of atmospheric aerosols. During severe haze pollution episodes, air quality
79 models often underestimate the extreme peak mass concentration of particulate matter
80 (Wang et al., 2014). Previous studies have revealed that the assimilation of atmospheric-
81 composition observations can improve air quality forecasts by constraining the
82 uncertainties of both the chemical ICs and emissions (Tang et al., 2010, 2011, 2013,
83 2016; Miyazaki et al., 2012, 2013, 2014). Peng et al. (2017) demonstrated that
84 significant improvements in forecasting PM_{2.5} can be achieved via the joint adjustment
85 of ICs and source emissions using an EnKF to assimilate surface PM_{2.5} observations.

86 In 2013, China launched an atmospheric environmental monitoring system that
87 provides real-time and online atmospheric chemical observations, including PM₁₀,
88 PM_{2.5}, SO₂, NO₂, O₃, and CO (<http://113.108.142.147:20035/emcpublish/>). This
89 dataset provides an opportunity to improve air quality forecasts using DA. However,



90 such fruitful observations are less used in air quality forecast despite of large
91 discrepancy existed between the forecast and observations. But it is now possible to
92 estimate the impact on forecast improvement of simultaneously assimilating various
93 surface observations. Thus, we developed an EnKF system that can simultaneously
94 assimilate surface measurements of PM₁₀, PM_{2.5}, SO₂, NO₂, O₃ and CO to correct WRF-
95 Chem (Weather Research and Forecasting model with Chemistry) forecasts using the
96 Goddard Chemistry Aerosol Radiation and Transport (GOCART) aerosol scheme. As
97 an extension to Peng et al. (2017), the impact of simultaneously assimilating various
98 surface aerosol and chemical observations was investigated.

99 Sections 2 and 3 briefly describe the DA system and observations used in this
100 study, respectively. The experimental design is introduced in Section 4. Finally, the
101 assimilation results are presented in Section 5, before a brief summary in Section 6.

102

103 2 DA system

104 The DA system in this study was the same as the one used in Peng et al. (2017). It
105 can simultaneously analyze the chemical ICs and emissions with the assimilation of
106 surface PM_{2.5} observations. A brief summary of the DA system is introduced here.

107 In every DA cycle, the ensemble emission scaling factors λ^f are first calculated
108 by the forecast model of scaling factors \mathbf{M}_{SF} (see details of \mathbf{M}_{SF} in section 2.2). Then,
109 the ensemble forecast emissions \mathbf{E}^f are calculated using the following equation:

$$110 \quad \mathbf{E}_{i,t} = \lambda_{i,t} \mathbf{E}_t^p, (i = 1, \dots, N), \quad (1)$$

111 where \mathbf{E}_t^p is the prescribed anthropogenic emission. The ensemble members of
112 chemical fields \mathbf{C}^f are forecasted using WRF-Chem, forced by the forecast emissions
113 \mathbf{E}^f whose ICs are previously analyzed concentration fields. Now, the background of
114 the joint vector, $\mathbf{x}^f = [\mathbf{C}^f, \lambda^f]^T$, has been produced. Then, the analyzed state vector,
115 $\mathbf{x}^a = [\mathbf{C}^a, \lambda^a]^T$, is optimized using an ensemble square root filter (EnSRF). Finally, the
116 assimilated emissions \mathbf{E}^a can be obtained using equation (1).

117

118 2.1 WRF-Chem model



119 The model used to simulate the transport of aerosols and chemical species was the
 120 WRF-Chem (Grell et al., 2005). As in Peng et al. (2017), we used version 3.6.1 and the
 121 physical and chemical parameterization options are listed in Table 1. The model
 122 computational domain covered almost the whole China and the horizontal resolution
 123 was 40.5 km. Figure 1b shows our area of interest, the North China Plain (NCP). The
 124 model included 57 vertical levels and the model top was 10 hPa.

125 The hourly prior anthropogenic emissions were based on the Multi-resolution
 126 Emission Inventory for China (MEIC) (Li et al., 2014) for October 2010, instead of the
 127 regional emission inventory in Asia (Zhang et al., 2009) for the year 2006 in Peng et al.
 128 (2017). The reason we chose the MEIC-2010 was that the total emissions are reasonable
 129 for cities over the NCP (Zheng et al., 2016). The original resolution of the MEIC-2010
 130 is $0.25^\circ \times 0.25^\circ$, but has been processed to match the model resolution (40.5 km) (Chen
 131 et al., 2016). No time variation was added to maintain objectivity in the prior
 132 anthropogenic emissions.

133

134 2.2 Forecast model of scaling factors

135 In this work, the primary sources to be optimized were the emissions of PM₁₀, PM_{2.5},
 136 SO₂, NO, NH₃ and CO. The sources of NH₃ were analyzed because they also impact
 137 greatly on the aerosols distribution. Thus, the emission scaling factors $\lambda_{i,t}^f =$
 138 ($\lambda_{\text{PM}_{2.5}}^f, \lambda_{\text{PM}_{10}}^f, \lambda_{\text{SO}_2}^f, \lambda_{\text{NO}}^f, \lambda_{\text{NH}_3}^f, \lambda_{\text{CO}}^f$) were prepared by the forecast model of scaling
 139 operator \mathbf{M}_{SF} before WRF-Chem integration.

140 We used the same persistence forecast operator \mathbf{M}_{SF} to forecast $\lambda_{i,t}^f$ as in Peng
 141 et al. (2017). The forecast operator was developed by using the ensemble forecast
 142 chemical fields. Thus,

$$143 \quad \kappa_{i,t} = \frac{c_{i,t}^f}{c_t^f}, (i = 1, \dots, N), \quad (2)$$

$$144 \quad (\kappa_{i,t})_{\text{inf}} = \beta(\kappa_{i,t} - \bar{\kappa}_t) + \bar{\kappa}_t, (i = 1, \dots, N), \quad (3)$$

$$145 \quad \lambda_{i,t}^p = (\kappa_{i,t})_{\text{inf}}, \quad (4)$$

$$146 \quad \lambda_{i,t}^f = \frac{1}{4}(\lambda_{i,t-3}^a + \lambda_{i,t-2}^a + \lambda_{i,t-1}^a + \lambda_{i,t}^p), (i = 1, \dots, N), \quad (5)$$



147 where $\mathbf{C}_{i,t}^f$ is the i th ensemble member of the chemical fields at time t , and $\overline{\mathbf{C}_t^f} =$
148 $\frac{1}{N} \sum_{i=1}^N \mathbf{C}_{i,t}^f$ is the ensemble mean; $\boldsymbol{\kappa}_{i,t}$ is the ensemble concentration ratios and $\overline{\boldsymbol{\kappa}_t}$ is
149 the ensemble mean of $\boldsymbol{\kappa}_{i,t}$ with values of 1; β is the inflation factor to keep the
150 ensemble spreads of $\boldsymbol{\kappa}_{i,t}$ at a certain level; $\boldsymbol{\lambda}_{i,t-1}^a$, $\boldsymbol{\lambda}_{i,t-2}^a$ and $\boldsymbol{\lambda}_{i,t-3}^a$ are the previous
151 assimilated emission scaling factors.

152 In this study, the ensemble forecast chemical fields of PM₂₅, PM₁₀, SO₂, NO, NH₃
153 and CO of the previous assimilation cycle are respectively used to calculate the
154 emission scaling factors ($\boldsymbol{\lambda}_{\text{PM}_{2.5}}^f, \boldsymbol{\lambda}_{\text{PM}_{10}}^f, \boldsymbol{\lambda}_{\text{SO}_2}^f, \boldsymbol{\lambda}_{\text{NO}}^f, \boldsymbol{\lambda}_{\text{NH}_3}^f, \boldsymbol{\lambda}_{\text{CO}}^f$). β is chosen as 1.3,
155 1.4, 1.3, 1.2, 1.2, and 1.4 for the ensemble concentration ratios of P₂₅, P₁₀, SO₂, NO,
156 NH₃ and CO, respectively in Equation (3).

157 Then, the sources $\mathbf{E}_{i,t}^f = (\mathbf{E}_{\text{PM}_{2.5}}^f, \mathbf{E}_{\text{PM}_{10}}^f, \mathbf{E}_{\text{SO}_2}^f, \mathbf{E}_{\text{NO}}^f, \mathbf{E}_{\text{NH}_3}^f, \mathbf{E}_{\text{CO}}^f)$ are calculated
158 using equation (1).

159 From the perspective of PM_{2.5} emissions, these include the unspiciated primary
160 sources of PM_{2.5} $\mathbf{E}_{\text{PM}_{2.5}}$, sulfate \mathbf{E}_{SO_4} , nitrate \mathbf{E}_{NO_3} , organic compounds \mathbf{E}_{org} and
161 elemental compounds \mathbf{E}_{BC} . We updated $\mathbf{E}_{\text{PM}_{2.5}}$, \mathbf{E}_{SO_4} and \mathbf{E}_{NO_3} (including the
162 nuclei and accumulation modes) following Peng et al. (2017).

163

164 2.3 DA algorithm

165 The assimilation algorithm employed was the EnSRF proposed by Whitaker and Hamill
166 (2002). The EnKF proposed by Evensen (1994) needs perturbations of observations in
167 practice. Compared to the original EnKF, the EnSRF obviates the need to perturb the
168 observations and avoids additional sampling errors introduced by perturbing
169 observations.

170 We used the same EnSRF as in Schwartz et al. (2012, 2014). The ensemble
171 member was chosen as 50. The localization radius was chosen as 607.5 km, so EnSRF
172 analysis increments were forced to zero at 607.5 km away from an observation (Gaspari
173 and Cohn, 1999). The posterior (after assimilation) multiplicative inflation factor was
174 chose as 1.2 for all the concentration analysis.



175

176 **2.4 State variables**

177 The DA system provides joint analysis of ICs and emissions following Peng et al.
178 (2017). Among them, 16 WRF-Chem/GOCART aerosol variables are included as the
179 state variables. Besides, chemical species, such as SO₂, NO₂ and O₃ are also included
180 because they are the most important gas-phase precursors or oxidants of the secondary
181 inorganic aerosols. CO is also assimilated because CO is an important tracer of
182 combustion sources, as well as a precursor of O₃ beyond NO₂ (Parrish et al., 1991). The
183 state variables of the emission scaling factors are $\lambda =$
184 $(\lambda_{\text{PM}_{2.5}}, \lambda_{\text{PM}_{10}}, \lambda_{\text{SO}_2}, \lambda_{\text{NO}}, \lambda_{\text{NH}_3}, \lambda_{\text{CO}})$.

185 Similar to weak-coupling DA, the DA system simultaneously updates both the ICs
186 and the emissions, but with no cross-variable update, in order to avoid the effects of
187 spurious multivariate correlations in the background error covariance that may develop
188 due to the limited ensemble size and errors in both the model and observations
189 (Miyazaki et al. 2012).

190 For the PM_{2.5} observations, the observation operator is expressed as (Schwartz et
191 al., 2012)

$$192 \quad y_{\text{pm}25}^f = \rho_d [\mathbf{P}_{25} + 1.375\mathbf{S} + 1.8(\mathbf{OC}_1 + \mathbf{OC}_2) + \mathbf{BC}_1 + \mathbf{BC}_2$$
$$193 \quad + \mathbf{D}_1 + 0.286\mathbf{D}_2 + \mathbf{S}_1 + 0.942\mathbf{S}_2], \quad (6)$$

194 where ρ_d is the dry air density; \mathbf{P}_{25} is the fine unspiculated aerosol contributions; \mathbf{S}
195 represents sulfate; \mathbf{OC}_1 and \mathbf{OC}_2 are hydrophobic and hydrophilic organic carbon
196 respectively; \mathbf{BC}_1 and \mathbf{BC}_2 are hydrophobic and hydrophilic black carbon respectively;
197 \mathbf{D}_1 and \mathbf{D}_2 are dusts with effective radii of 0.5 and 1.4 μm respectively; \mathbf{S}_1 and \mathbf{S}_2 are
198 sea salts with effective radii of 0.3 and 1.0 μm respectively. In fact, PM_{2.5} observations
199 were only used to analyze \mathbf{P}_{25} , \mathbf{S} , \mathbf{OC}_1 , \mathbf{OC}_2 , \mathbf{BC}_1 , \mathbf{BC}_2 , \mathbf{D}_1 , \mathbf{D}_2 , \mathbf{S}_1 , \mathbf{S}_2 and $\lambda_{\text{PM}_{2.5}}$. Since
200 we had no NH₃ observations, PM_{2.5} observations were also used to analyze λ_{NH_3} (see
201 Table 2). For other control variables, PM_{2.5} observations were not allowed to alter them.

202 For the PM₁₀ observations, the PM₁₀ observation operator is expressed as (Jiang
203 et al., 2013)



$$y_{\text{pm}10}^f = \rho_d[\mathbf{P}_{10} + \mathbf{P}_{25} + 1.375\mathbf{S} + 1.8(\mathbf{OC}_1 + \mathbf{OC}_2) + \mathbf{BC}_1 + \mathbf{BC}_2 + \mathbf{D}_1 + 0.286\mathbf{D}_2 + \mathbf{D}_3 + 0.87\mathbf{D}_4 + \mathbf{S}_1 + 0.942\mathbf{S}_2 + \mathbf{S}_3]. \quad (7)$$

206 Thus,

$$y_{\text{pm}10-2.5}^f = \rho_d[\mathbf{P}_{10} + \mathbf{D}_3 + 0.87\mathbf{D}_4 + \mathbf{S}_3], \quad (8)$$

208 meaning that, in the assimilation experiments, we did not use the PM_{10} observations
209 directly. In equation (13) and (14), P_{10} denotes the coarse-mode unspicinated aerosol
210 contributions; D_3 and D_4 are dusts with effective radii of 2.4 and 4.5 μm respectively;
211 S_3 is sea salt with effective radii of 3.25 μm . We used the $\text{PM}_{10-2.5}$ observations (the
212 differences between the PM_{10} observations and the $\text{PM}_{2.5}$ observations, $y_{\text{pm}10-2.5}^o =$
213 $y_{\text{pm}10}^o - y_{\text{pm}10}^o$) to analyze P_{10} , D_3 , D_4 , S_3 and $\lambda_{\text{PM}10}$. In addition, $\text{PM}_{10-2.5}$
214 observations were used to analyze D_5 and S_4 , since they are coarse-mode mineral dust
215 and sea salt aerosols. $\text{PM}_{10-2.5}$ observations were not allowed to impact other control
216 variables.

217 Moreover, as shown in Table 2, SO_2 observations were used to analyze the SO_2
218 concentration and λ_{SO_2} . NO_2 observations were used to estimate the NO , NO_2
219 concentration and λ_{NO} . CO observations were used to analyze the CO concentration
220 and λ_{CO} . And finally, O_3 observations were only used to analyze the O_3 concentration.
221

222 3. Observations and errors

223 The surface chemical observations used in this study were obtained from the Ministry
224 of Ecology and Environment of China. Altogether, there were 876 observational sites
225 over the model domain (Figure 1). At most sites, one measurement was selected
226 randomly for the assimilation experiment on a $0.1^\circ \times 0.1^\circ$ grid. Altogether, 355 stations
227 were kept for the model domain, where 133 assimilation stations were located on the
228 NCP and 40 stations were located in the Beijing–Tianjin–Hebei (BTH) region. Other
229 stations were used for verification purposes: 167 independent stations were located on
230 the NCP and 47 in the BTH region.

231 The observation error covariance matrix \mathbf{R} included measurement errors and



232 representation errors. We assumed that \mathbf{R} is a diagonal matrix (without observation
233 correlation).

234 Following Elbern et al. (2007), the measurement error ε_0 is defined as

$$235 \quad \varepsilon_0 = a + b * \Pi_0, \quad (9)$$

236 where Π_0 represents the measurements for $\text{PM}_{2.5}$, $\text{PM}_{10-2.5}$, SO_2 , NO_2 , CO or O_3 (units:
237 $\mu\text{g m}^{-3}$). A value of $a = 1.5$ and $b = 0.0075$ was chosen for $\text{PM}_{2.5}$, $\text{PM}_{10-2.5}$, SO_2 ,
238 and NO_2 . For CO , $a = 10$ and $b = 0.0075$.

239 The representativeness error is defined as

$$240 \quad \varepsilon_r = r\varepsilon_0\sqrt{\Delta x/L}, \quad (10)$$

241 where $r = 0.5$, $\Delta x = 40.5$ km (the model resolution), and $L = 3$ km due to the
242 lack of the information of the station type (Elbern et al., 2007).

243 Finally, the total error (ε_t) is defined as

$$244 \quad \varepsilon_t = \sqrt{\varepsilon_0^2 + \varepsilon_r^2}, \quad (11)$$

245 In order to ensure data reliability, the observations were subjected to quality
246 control before DA. Data values larger than a certain threshold were classified as
247 unrealistic and were not assimilated. The threshold values were chosen as 700, 800,
248 300, 300, 400 and 4000 $\mu\text{g m}^{-3}$ for $\text{PM}_{2.5}$, $\text{PM}_{10-2.5}$, SO_2 , NO_2 , O_3 and CO , respectively.
249 In addition, observations leading to innovations exceeding a certain value were also
250 omitted. These threshold values were chosen as 70 $\mu\text{g m}^{-3}$ for $\text{PM}_{2.5}$, $\text{PM}_{10-2.5}$, SO_2 ,
251 NO_2 and O_3 . Also, 1500 $\mu\text{g m}^{-3}$ was chosen for CO .

252

253 **4. Experimental design**

254 The DA experiment followed that of Peng et al. (2017), in which the assimilation
255 of pure surface $\text{PM}_{2.5}$ measurements with the EnKF was performed to correct finer
256 aerosol variables and associated emissions. The experiment focused on an extreme haze
257 event that occurred in October 2014 over North China. The 50-member ensemble spin-
258 up forecasts were performed from 1 to 4 October 2014, in which the ICs, the lateral
259 boundary conditions and the emissions are perturbed by adding random noise. Then,
260 the observed PM_{10} , $\text{PM}_{2.5}$, SO_2 , NO_2 , O_3 and CO data starting from 5 to 16 October



261 were assimilated hourly to adjust the ICs and the corresponding emissions.

262 After that, two sets of 72-h forecasts were performed, each at 00:00 UTC from 6
263 to 15 October 2014, with hourly forecasting outputs for the assimilation experiment.

264 These two sets of forecasting experiments were conducted using the ensemble mean of
265 the concentration analysis as the ICs. One set of the experiments was forced by the
266 optimized emissions (denoted as fcICsEs), and the other was forced by the prescribed
267 anthropogenic emissions (denoted as fcICs). The aim was to use the difference between
268 the fcICsEs and fcICs to indicate the impact of the optimized emissions.

269 Moreover, we also run a control experiment. The ICs were based on the ensemble
270 mean of the spin-up forecasts at 00:00 UTC on 5 October 2014. The emissions were
271 the prescribed emissions.

272

273 5. Results

274 5.1 Ensemble performance

275 We begin by assessing the ensemble performance for the DA system. Figure 2 shows
276 the time series of the prior total spreads and the prior root-mean-square errors (RMSEs)
277 for PM_{2.5}, PM₁₀, and the four trace gases calculated against all observations in the BTH
278 region. It shows that the magnitudes of the total spreads were close to the RMSEs,
279 indicating that the DA system was well calibrated (Houtekamer et al., 2005).

280 Figure 3 shows the area-averaged time series extracted from the ensemble spread
281 of the six emission scaling factors ($\lambda_{\text{PM}_{2.5}}^f$, $\lambda_{\text{PM}_{10}}^f$, $\lambda_{\text{SO}_2}^f$, λ_{NO}^f , $\lambda_{\text{NH}_3}^f$ and λ_{CO}^f) in the
282 BTH region. It shows that the ensemble spread of all the scaling factors were very stable
283 throughout the ~10-day experiment period, which indicates that \mathbf{M}_{SF} can generate
284 stable artificial data to generate the ensemble emissions. The value of the emission
285 scaling factors ranged from 0.2 to 0.6, indicating that the uncertainty of the assimilated
286 emissions was about 20%–60%.

287

288 5.2 Forecast improvements

289 In order to evaluate the overall performance of the DA system, time series of the hourly
290 pollutant concentrations from the control run, the analysis, and the first-day forecast of



291 the two forecasting experiments were compared with the independent observations in
292 the BTH region (Figure 4). Besides, model evaluation statistics (Table 3) were
293 calculated against independent observations from 6 to 16 October 2014. In addition,
294 biases and RMSEs were presented as a function of forecast range for the control,
295 analysis, and forecast experiments (Figures 5–7).

296 The control run did not perform very well, although it could capture the synoptic
297 variability and reproduce the overall pollutant levels when there was a severe haze event.
298 The statistics show that there were larger systematic biases and RMSEs and a smaller
299 correlation coefficient (CORR) for the control (see Table 3). The biases were -34.1 ,
300 -77.7 , -565.7 and $-31 \mu\text{g}\cdot\text{m}^{-3}$ for $\text{PM}_{2.5}$, PM_{10} , CO , and O_3 , respectively, from 6 to 16
301 October—about 29.7%, 44.5%, 42.9% and 53.9% lower than the corresponding
302 observed concentrations. During the severe haze episode from 8 to 10 October in
303 particular, when observed $\text{PM}_{2.5}$ were larger than $200 \mu\text{g}\cdot\text{m}^{-3}$, the biases reached -90.5 ,
304 -143.1 , -911.8 and $-39.1 \mu\text{g}\cdot\text{m}^{-3}$, respectively—about 44.4%, 51.9%, 49.2% and 55.7%
305 lower than the corresponding observed concentrations, suggesting a significant
306 systematic underestimation of the WRF-Chem simulation. Additionally, a significant
307 overestimation of $48.1 \mu\text{g}\cdot\text{m}^{-3}$ was obtained for SO_2 —about 145.8% higher than the
308 observed concentrations. As for the NO_2 simulation, WRF-Chem was able to
309 realistically describe the diurnal and synoptic evolution of NO_2 concentrations. The
310 model bias was $22.4 \mu\text{g}\cdot\text{m}^{-3}$, which was about 39.7% higher than the observed NO_2 .
311 These results were similar to the simulations of Chen et al. (2016). Most of the WRF-
312 Chem settings used here were the same as those used in Chen et al. (2016), except that
313 they used CBMZ (Carbon Bond Mechanism, version Z) and MOSAIC (Model for
314 Simulating Aerosol Interactions and Chemistry) as the gas-phase and aerosol chemical
315 mechanisms.

316 After the assimilation of surface observations, the time series of the hourly
317 pollutant concentrations from the analysis showed much better agreement with
318 observations than those from the control. The magnitudes of the bias and the RMSEs
319 decreased and the CORRs increased for all six species. The biases were 5.1, -5.6 , 8.1,
320 -8.3 , -160.4 and $2.1 \mu\text{g}\cdot\text{m}^{-3}$ for $\text{PM}_{2.5}$, PM_{10} , SO_2 , NO_2 , CO and O_3 , respectively—



321 about 4.4%, -3.2%, 24.5%, -14.7%, -12.17% and 3.7% of the corresponding observed
322 concentrations, indicating that the analysis fields were very close to the observations.
323 The RMSEs were 51.5, 63.4, 27.9, 31.7, 618.9 and 31.1 $\mu\text{g m}^{-3}$, respectively—about
324 44.1%, 52.9%, 58.1%, 20.2%, 35.7% and 38.78% lower than the RMSEs of the control
325 run. The CORRs reached 0.891, 0.890, 0.540, 0.557, 0.705 and 0.753, respectively.
326 These statistics indicate that the DA system was able to adjust the chemical ICs
327 efficiently.

328 The $\text{PM}_{2.5}$, PM_{10} and CO concentrations from both sets of forecasting experiments
329 benefitted substantially from the DA procedure, as expected. Smaller biases and
330 RMSEs were obtained for almost the entire 72-h forecast range (see Figures 5–7), as
331 compared with the control run. For the first-day forecast in particular, the model
332 performed almost perfectly. It faultlessly captured the diurnal and synoptic variability
333 of the pollutant (see figure 4), in a manner that was very close to that of the analysis.
334 The overall biases were 6.5, -11.9 and 100.4 $\mu\text{g m}^{-3}$ for $\text{PM}_{2.5}$, PM_{10} and CO,
335 respectively; and the RMSEs were 77.8, 98.7 and 805.1 $\mu\text{g m}^{-3}$, respectively, in
336 fcICsEs24 (see Table 3). In fcICs24, the biases were 8.3, -10.3 and 130.2 $\mu\text{g m}^{-3}$,
337 respectively; and the RMSEs were 75.1, 95.9 and 838.2 $\mu\text{g m}^{-3}$, respectively (see Table
338 3). However, with longer-range forecasts, the impact of DA quickly decayed. The
339 relative reductions in RMSE mostly ranged from 30% to 5% for the second- and third-
340 day forecast. From the perspective of the impact of the assimilated emissions, fcICs
341 performed similarly to fcICsEs for $\text{PM}_{2.5}$, PM_{10} and CO, indicating that ICs play key
342 roles in aerosol and CO forecasts during severe haze episodes, while the impact of
343 assimilated emissions seems negligible.

344 For the SO_2 verification forecast, however, fcICsEs performed much better than
345 both fcICs and the control run. Smaller biases and RMSEs were obtained for almost the
346 entire 72-h forecast range. At nighttime in particular (from 18 to 23 h, 42 to 47 h, and
347 66 to 73 h), when there was significant systematic overestimation in the control run,
348 both the biases and the RMSEs in fcICsEs were about 30% lower than those of the
349 control run. During the daytime (from 0 to 9 h, 24 to 33 h, and 48 to 57 h), fcICsEs still
350 performed slightly better, although the control run did a near perfect job. As for fcICs,



351 smaller biases and RMSEs were obtained for only the first 3 h. Then, the performance
352 was the same as the control run, indicating that the impact of the ICs had disappeared.
353 These results demonstrate the superiority of the assimilated emissions, and that the joint
354 adjustment of SO₂ ICs and emissions is an efficient way to improve the SO₂ forecast.

355 The NO₂ DA results for the independent sites showed really poor performance
356 (see Figures 5–7). Smaller biases were gained in the daytime of the experiment trials.
357 At nighttime, however, when the simulated NO₂ deviated considerably from the
358 observations in the control run, the biases of both sets of the validation forecasts became
359 even larger. Besides, almost all the RMSEs of both sets of the validation forecasts were
360 always larger than those of the control run.

361 The O₃ DA results were dependent on the NO₂ DA results in the daytime, due to
362 chemical transformation. Both the biases and the RMSEs were larger, as compared with
363 those of the control run (see Figures 5–7). However, at nighttime, when there was
364 significant systematic underestimation in the control run, the biases in fcICsEs had very
365 similar values to those of the analysis. Also, the biases in fcICs ranged between the
366 analysis and the control run; and the RMSEs of both sets of forecasting experiments
367 were about 10% smaller than those of the control run. All these results indicate that the
368 DA system performed well at night.

369

370 5.3 Emission optimization results

371 Besides improved pollutant forecasts, improved estimates of emissions were expected
372 from the joint DA procedure. The MEIC-2010 was constructed on the basis of annual
373 statistical books in which the data were often 2–3 years older than the actual year (Chen
374 et al., 2016). However, consistent efforts aimed at reducing and managing
375 anthropogenic emissions have been made over the past decade to mitigate air pollution.
376 Thus, there was a large difference between the emission year and our simulation year.
377 Besides, the spatial allocations of these emissions over small spatial scales, and the
378 monthly allocations, will also lead to some uncertainties. Lastly, the emissions
379 inventory cannot fully capture the day-to-day variability or the actual daily variations,
380 though its differentiation in terms of working days and weekend days, plus the daily



381 variations, can be taken into account in practical applications. However, in this
382 assimilation procedure, the differentiation in terms of working days and weekend days,
383 plus the daily variations, was ignored. Therefore, the prescribed anthropogenic
384 emissions were subject to large uncertainties.

385 Figures 8 and 9 display the spatial distribution of the prescribed emission rates and
386 the differences between the analysis and the prescribed emission rates of PM_{2.5}, PM₁₀,
387 NH₃, SO₂, NO and CO averaged over all hours from 6 to 16 October 2014 in the NCP
388 region. The assimilated emission rates of PM_{2.5}, SO₂, NO and CO were lower than the
389 prescribed emissions on the whole. In the BTH region especially, the differences
390 reached $-0.02 \mu\text{g}\cdot\text{m}^{-2}\cdot\text{s}^{-1}$, -2.9 , -8.8 and $-24.65 \text{ mol}\cdot\text{km}^{-2}\cdot\text{hr}^{-1}$, which was a reduction
391 of about 10%–20% of the prescribed emissions. For PM₁₀ emissions, the assimilated
392 values were very close to the prescribed ones, indicating that the prescribed PM₁₀
393 emissions had small uncertainties for the NCP region. For NH₃ emissions, the
394 assimilated values were a little larger than the prescribed emissions in large industrial
395 cities like Beijing, Tianjin, Baoding, Xingtai, Handan, and Taiyuan. However, they
396 were smaller than the prescribed emissions in agricultural regions, especially in
397 Shandong Province and Henan Province. However, in the BTH region, the assimilated
398 NH₃ emissions were very close to the prescribed emissions on the whole.

399 Figure 10 shows the time series of the emission scaling factors and the emissions.
400 As concluded in Peng et al. (2017), the forecast emission scaling factors changed with
401 the analyzed emission scaling factors due to the use of the time smoothing operator.
402 Besides, although the prescribed emissions were constant when designing the
403 assimilation experiment, the analyzed emission scaling factors showed obvious
404 variation with time, as did the analyzed emissions. For the assimilated SO₂ and NO
405 emissions in particular, the diurnal variations were perfect. In addition, the difference
406 between the assimilated emissions and the prescribed emissions were consistent with
407 those in Figures 8 and 9. The assimilated emissions of PM_{2.5}, SO₂, NO and CO were
408 apparently lower than the corresponding prescribed emissions. Whereas, the values of
409 the assimilated emissions of PM₁₀ and NH₃ were very close to their corresponding
410 prescribed emissions.



411

412 5.4 Discussion

413 From the results presented above, it is clear that improvements were achieved for
414 almost all the 72-h verification forecasts using the optimized ICs and emissions for
415 PM_{2.5}, PM₁₀, SO₂ and CO concentrations in the BTH region. However, the 72-h NO₂
416 verification forecasts performed much worse than the control run, due to the
417 assimilation. Plus, the 72-h O₃ verification forecasts performed worse than the control
418 run during the daytime, due to the worse performance of the NO₂ forecasts, although
419 they did perform better at night. However, relatively favorable NO₂ and O₃ forecast
420 results were gained for the Yangtze River delta and Pearl River delta (PRD) regions
421 (see Figure 11). In the PRD region, during the daytime, the three NO₂ forecasts (i.e.,
422 the control run, the fcICsEs, and the fcICs) performed similarly, and had relatively
423 small biases and RMSEs. At nighttime, when there was significant systematic
424 overestimation in the control run, the biases and the RMSEs in fcICsEs were much
425 smaller than those in the control run. For the O₃ 72-h verification forecasts, fcICsEs
426 performed much better than the control run, except for the first 8 h. Also, fcICs
427 improved the O₃ forecasts to some extent from the 9- to 72-h forecast range. These
428 results indicate that DA is still an effective way to improve NO₂ and O₃ forecasts.

429 Regarding the failure to improve the NO₂ and O₃ forecasts in the BTH region,
430 there are three likely factors. And certainly, NO₂ and O₃ forecasts in other areas are also
431 facing similar challenges.

432 Firstly, there are still some limitations for the EnKF method. EnKF assimilation is
433 influenced greatly by model errors and observation errors. For short-lived chemical
434 reactive species, such as NO₂ and O₃, they undergo highly complex nonlinear
435 photochemical reactions, even on timescales of hours, such that the forecast accuracy
436 is largely dependent on the chemical process as well as the physical transportation
437 process, the ICs, and the emissions. However, those complex photochemical reaction
438 processes are not precisely described in current chemical mechanisms, e.g.,
439 heterogeneous reactions (Yang et al., 2015), the photolysis of nitrous acid and ClNO₂
440 during daytime (Zhang et al., 2017), and so on. Therefore, on the one hand, there are



441 still large uncertainties for NO₂ and O₃ forecasts; whilst on the other hand, it is very
442 difficult for NO₂ and O₃ DA to accurately estimate the model errors with a limited
443 ensemble size. Thus, NO₂ and O₃ assimilations do not perform well (Elbern et al., 2007;
444 Tang et al., 2016). However, for SO₂ and CO, which are representative of long-lived
445 chemical reactive species, the chemical reaction process does not work
446 on timescales of hours, meaning that to some extent hourly chemical DA has the
447 potential to improve their forecasts. For CO in particular, due to its inertness, we might
448 be able to obtain high-quality ICs and emissions through DA. The primary sources of
449 aerosol are the dominant part of the atmospheric aerosol concentration. So, 72-h aerosol
450 forecasts may perform similarly to CO, albeit there are large uncertainties in the
451 chemical model.

452 Secondly, the analysis ICs and emissions are only a mathematical optimum under
453 the existing conditions. Only part of the chemical ICs and emissions are involved in the
454 DA experiment; and VOC ICs and emissions, which may greatly influence the NO₂ and
455 O₃ forecasts, were not included here because of the absence of VOC measurements.
456 Although we carried out two DA sensitivity experiments to adjust the VOC ICs and
457 emissions through the use of NO₂ or O₃ measurements, we were still unable to gain
458 improved NO₂ and O₃ forecasts in the BTH region in both DA experiments. VOC
459 measurements are needed to reduce uncertainties of VOC ICs and emissions. In
460 addition, almost all available data were observed in cities, and no observation stations
461 located in rural. Thus, the atmospheric environmental monitoring system was still
462 spatially heterogeneous.

463 Another important point is that there are still limitations to the current chemical
464 mechanisms used in our model, such as the treatment of model error. NO is the primary
465 species of NO_x emissions in city areas, and reacts directly with O₃ to form NO₂ (NO+O₃
466 →NO₂+O₂). Thus, O₃ concentrations may inversely correlate with NO₂ concentrations
467 at night. Consequently, air quality models may systematically underestimate O₃
468 concentrations. Currently, DA can only revise the ICs and the emissions in this work. It
469 cannot change the model performance, especially when there are certain uncertainties
470 for the meteorological simulation.



471

472 **6. Summary**

473 In this study, we developed an EnKF system to simultaneously assimilate surface
474 measurements of PM₁₀, PM_{2.5}, SO₂, NO₂, O₃ and CO via the joint adjustment of ICs
475 and source emissions. This system was applied to assimilate hourly pollution data while
476 modeling an extreme haze event that occurred in early October 2014 over North China.
477 In order to evaluate the impact of DA, two sets of 72-h verification forecasts were
478 performed. One was conducted with the optimized ICs and emissions, and the other
479 with only optimized ICs and the prescribed emissions. A control experiment without
480 DA was also performed for comparison.

481 The results showed that both verification forecasts performed much better than the
482 control simulations for PM_{2.5}, PM₁₀ and CO. Obvious improvements were achieved for
483 almost the entire 72-h forecast range. For the first-day forecast especially, near perfect
484 forecasts results were achieved. However, with longer-range forecasts, the impact of
485 DA quickly decayed. In addition, the forecasts with only optimized ICs and the
486 prescribed emissions performed similarly to that with the optimized ICs and emissions,
487 indicating that ICs play key roles in PM_{2.5}, PM₁₀ and CO forecasts during severe haze
488 episodes.

489 Also, large improvements were achieved for SO₂ forecasts with both the optimized
490 ICs and emissions for the whole 72-h forecast range. However, similar improvements
491 were achieved for SO₂ forecasts with the optimized ICs only for just the first 3 h, and
492 then the impact of the ICs decayed quickly to zero. This demonstrates that the joint
493 adjustment of SO₂ ICs and emissions is an efficient way to improve SO₂ forecasts.

494 Even though we failed to improve the NO₂ and O₃ forecasts in the BTH region,
495 relatively favorable NO₂ and O₃ forecast results were gained in other areas. Also, the
496 forecasts with both the optimized ICs and emissions performed much better than the
497 forecasts with only optimized ICs and the prescribed emissions. These results indicate
498 that there is still potential to improve NO₂ and O₃ forecasts via the joint adjustment of
499 SO₂ ICs and emissions.

500

501 **References**

- 502 Barbu, A. L., Segers, A. J., Schaap, M., Heemink, A.W., and Builtjes, P. J. H.: A multi-component data assimilation
503 experiment directed to sulphur dioxide and sulphate over Europe, *Atmos. Environ.*, 43, 1622–1631, 2009.
- 504 Carmichael, G. R., Daescu, D. N., Sandu, A., and Chai, T.: Computational aspects of chemical data assimilation into
505 atmospheric models, in *Science Computational ICCS 2003. Lecture Notes in Computer Science, IV*, 269–278,
506 Springer, Berlin, 2003.
- 507 Carmichael, G. R., Sandu, A., Chai, T., Daescu, D. N., Constantinescu, E. M., and Tang, Y.: Predicting air quality:
508 improvements through advanced methods to integrate models and measurements, *J. Comput. Phys.*, 227, 3540–
509 3571, 2008a.
- 510 Carmichael, G. R., Sakuraib, T., Streetsc, D., Hozumib, Y., Uedab, H., Parkd, S. U., Funge, C., Hanb, Z., Kajinof,
511 M., Engardt, M., Bennetg, C., Hayamih, H., Sarteleti, K., Hollowayj, T., Wangk, Z., Kannaril, A., Fum, J.,
512 Matsudan, K., Thongboonchooa, N., and Amanno, M.: MICS-ASIA II: the model intercomparison study for
513 Asia phase II methodology and overview of findings, *Atmos. Environ.*, 42, 3468–3490, 2008b.
- 514 Chai, T., Carmichael, G. R., Tang, Y., Sandu, A., Hardesty, M., Pilewskie, P., Whitlow, S., Browell, E. V., Avery,
515 M. A., Nedelec, P., Merrill, J. T., Thompson, A. M., and Williams, E.: Four dimensional data assimilation
516 experiments with International Consortium for Atmospheric Research on Transport and Transformation ozone
517 measurements, *J. Geophys. Res.*, 112, D12S15, doi:10.1029/2006JD007763, 2007.
- 518 Chen, D., Liu, Z., Fast, J., and Ban, J.: Simulations of sulfate – nitrate – ammonium (SNA) aerosols during the
519 extreme haze events over northern China in October 2014, *Atmos. Chem. Phys.*, 16, 10707 – 10724,
520 doi:10.5194/acp-16-10707-2016, 2016.
- 521 Chen, F. and Dudhia, J.: Coupling an advanced land surface hydrology model with the Penn State-NCAR MM5
522 modeling system. Part I: Model implementation and sensitivity, *Mon. Weather Rev.*, 129, 569 – 585,
523 doi:10.1175/1520-0493(2001)129<0569:Caalsh>2.0.Co;2, 2001.
- 524 Chin, M., Rood, R. B., Lin, S. J., Muller, J. F., and Thompson, A. M.: Atmospheric sulfur cycle simulated in the
525 global model GOCART: Model description and global properties, *J. Geophys. Res.-Atmos.*, 105, 24671 –
526 24687, 2000.
- 527 Chin, M., Ginoux, P., Kinne, S., Torres, O., Holben, B. N., Duncan, B. N., Martin, R. V., Logan, J. A., Higurashi,
528 A., and Nakajima, J.: Tropospheric aerosol optical thickness from the GOCART model and comparisons with
529 satellite and Sun photometer measurements, *J. Atmos. Sci.*, 59, 461 – 483, 2002.
- 530 Chou, M.-D. and Suarez, M. J.: An efficient thermal infrared radiation parameterization for use in general circulation
531 models, *NASA Tech. Memo.*, TM 104606, vol. 3, 25 pp., NASA Goddard Space Flight Cent., Greenbelt, MD,
532 USA, 1994.
- 533 Dai, T., Schutgens, N. A. J., Goto, D., Shi, G. Y., and Nakajima, T.: Improvement of aerosol optical properties
534 modeling over Eastern Asia with MODIS AOD assimilation in a global non-hydrostatic icosahedral aerosol
535 transport model, *Environ. Pollut.*, 195, 319–329, 2014.
- 536 Ding, A. J., Huang, X., Nie, W., Sun, J., Kerminen, V. M., Petaja, T., Su, H. L., Cheng, Y. F., Yang, X. Q., and
537 Wang, M.: Enhanced haze pollution by black carbon in megacities in China, *Geophys. Res. Lett.*, 2873–2879,
538 doi:10.1002/2016GL067745, 2016.
- 539 Ding, J., van der A, R. J., Mijling, B., Levelt, P. F., and Hao, N.: NO_x emission estimates during the 2014 Youth
540 Olympic Games in Nanjing, *Atmos. Chem. Phys.*, 15, 9399–9412, doi:10.5194/acp-15-9399-2015, 2015.
- 541 Elbern, H., Schmidt, H., and Ebel, A.: Variational data assimilation for tropospheric chemistry modelling, *J. Geophys.*
542 *Res.*, 102, 15967–15985, 1997.
- 543 Elbern, H. and Schmidt, H.: A 4D-Var chemistry data assimilation scheme for Eulerian chemistry transport
544 modelling, *J. Geophys. Res.*, 104, 18583–18598, 1999.



- 545 Elbern, H., Schmidt, H., Talagrand, O., and Ebel, A.: 4D-variational data assimilation with an adjoint air quality
546 model for emission analysis, *Environ. Model. Softw.*, 15, 539–548, 2000.
- 547 Elbern, H. and Schmidt, H.: Ozone episode analysis by four dimensional variational chemistry data assimilation, *J.*
548 *Geophys. Res.*, 106, 3569–3590, 2001.
- 549 Elbern, H., Strunk, A., Schmidt, H., and Talagrand, O.: Emission rate and chemical state estimation by 4-dimensional
550 variational inversion, *Atmos. Chem. Phys.*, 7, 3749–3769, doi:10.5194/acp-7-3749-2007, 2007.
- 551 Evensen, G.: Sequential data assimilation with a nonlinear quasigeostrophic model using Monte Carlo methods to
552 forecast error statistics, *J. Geophys. Res.*, 99, 10143 – 10162, 1994.
- 553 Gaspari, G. and Cohn S. E.: Construction of correlation functions in two and three dimensions, *Quart. J. R. Meteorol.*
554 *Soc.* 125 (1999), 723–757.
- 555 Ginoux, P., Chin, M., Tegen, I., Prospero, J. M., Holben, B., Dubovik, O., and Lin, S.-J.: Sources and distributions
556 of dust aerosols simulated with the GOCART model, *J. Geophys. Res.*, 106, 20255 – 20273,
557 doi:10.1029/2000JD000053, 2001.
- 558 Grell, G., Peckham, S. E., Schmitz, R., McKeen, S. A., Frost, G., Skamarock, W. C., and Eder, B.: Fully coupled
559 “ online ” chemistry within the WRF model, *Atmos. Environ.*, 39, 6957 – 6975,
560 doi:10.1016/j.atmosenv.2005.04.027, 2005.
- 561 Guenther, A., Hewitt, C. N., Erickson, D., Fall, R., Geron, C., Graedel, T., Harley, P., Klinger, L., Lerdau, M.,
562 McKay, W., Pierce, T., Scholes, B., Steinbrecher, R., Tallamraju, R., Taylor, J., and Zimmerman, P.: A global
563 model of natural volatile organic compound emissions, *J. Geophys. Res.*, 100, 8873 – 8892,
564 doi:10.1029/94JD02950, 1995.
- 565 Guerrette, J. J. and Henze, D. K.: Development and application of the WRFPLUS-Chem online chemistry adjoint
566 and WRFDA-Chem assimilation system, *Geosci. Model Dev.*, 8, 1857–1876, doi:10.5194/gmd-8-1857-2015,
567 2015.
- 568 Hakami, A., Henze, D. K., Seinfeld, J. H., Chai, T., Tang, Y., Carmichael, G. R., and Sandu, A.: Adjoint inverse
569 modeling of black carbon during the Asian Pacific Regional Aerosol Characterization Experiment, *J. Geophys.*
570 *Res.-Atmos.*, 110, D14301, doi:10.1029/2004JD005671, 2005.
- 571 Heemink, A. W. and Segers, A. J.: Modeling and prediction of environmental data in space and time using Kalman
572 filtering, *Stoch. Environ. Res. Risk A.*, 16, 225–240, 2002.
- 573 Henze, D. K., Hakami, A., and Seinfeld, J. H.: Development of the adjoint of GEOS-Chem, *Atmos. Chem. Phys.*, 7,
574 2413–2433, doi:10.5194/acp-7-2413-2007, 2007.
- 575 Henze, D. K., Seinfeld, J. H., and Shindell, D. T.: Inverse modeling and mapping US air quality influences of
576 inorganic PM_{2.5} precursor emissions using the adjoint of GEOS-Chem, *Atmos. Chem. Phys.*, 9, 5877–5903,
577 doi:10.5194/acp-9-5877-2009, 2009.
- 578 Hong, S. Y., Noh, Y., and Dudhia, J.: A new vertical diffusion package with an explicit treatment of entrainment
579 processes, *Mon. Weather Rev.*, 134, 2318–2341, doi:10.1175/Mwr3199.1, 2006.
- 580 Houtekamer, P. L., Mitchell, H. L., Pellerin, G., Buehner, M., Charron, M., Spacek, L., and Hansen, B.: Atmospheric
581 data assimilation with an ensemble Kalman filter: Results with real observations, *Mon. Weather Rev.*, 133,
582 604 – 620, 2005.
- 583 Huang, X., Song, Y., Zhao, C., Li, M., Zhu, T., Zhang Q., and Zhang, X. Y.: Pathways of sulfate enhancement by
584 natural and anthropogenic mineral aerosols in China, *J. Geophys. Res. – Atmos.*, 119, 24, 14165–14179, 2014.
- 585 Jiang, Z., Liu, Z., Wang, T., Schwartz, C. S., Lin, H.-C., and Jiang, F.: Probing into the impact of 3DVAR
586 assimilation of surface PM₁₀ observations over China using process analysis, *J. Geophys. Res.-Atmos.*, 118,
587 6738–6749, doi:10.1002/jgrd.50495, 2013.
- 588 Li, Z., Zang, Z., Li, Q. B., Chao, Y., Chen, D., Ye, Z., Liu, Y., and Liou, K. N.: A three-dimensional variational data



- 589 assimilation system for multiple aerosol species with WRF/Chem and an application to PM_{2.5} prediction, Atmos.
590 Chem. Phys., 13, 4265–4278, doi:10.5194/acp-13-4265-2013, 2013.
- 591 Li, M., Zhang, Q., Streets, D. G., He, K. B., Cheng, Y. F., Emmons, L. K., Huo, H., Kang, S. C., Lu, Z., Shao, M.,
592 Su, H., Yu, X., and Zhang, Y.: Mapping Asian anthropogenic emissions of nonmethane volatile organic
593 compounds to multiple chemical mechanisms, Atmos. Chem. Phys., 14, 5617 – 5638, doi:10.5194/acp-14-
594 5617-2014, 2014
- 595 Liu, Z., Liu, Q., Lin, H. C., Schwartz, C. S., Lee, Y. H., and Wang, T.: Three-dimensional variational assimilation
596 of MODIS aerosol optical depth: implementation and application to a dust storm over East Asia, J. Geophys.
597 Res., 116, D23206, doi:10.1029/2011JD016159, 2011.
- 598 McLinden, C.A., Fioletov, V., Shephard, M.W., Krotkov, N., Li, C., Martin, R.V., Moran, M.D., and J. Joiner.: Space-
599 based detection of missing sulfur dioxide sources of global air pollution, Nat. Geosci., 9, 496–500,
600 doi:10.1038/ngeo2724, 2016.
- 601 Mijling, B., van der A, R. J., Boersma, K. F., Van Roozendaal, M., De Smedt, I., and Kelder, H. M.: Reduction of
602 NO₂ detected from space during the 2008 Beijing Olympic Games, Geophys. Res. Lett., 36, L13801,
603 doi:10.1029/2009GL038943, 2009.
- 604 Mijling, B. and van der A, R. J.: Using daily satellite observations to estimate emissions of short-lived air pollutants
605 on a mesoscopic scale, J. Geophys. Res., 117, D17302, doi:10.1029/2012JD017817, 2012.
- 606 Mijling, B., van der A, R. J., and Zhang, Q.: Regional nitrogen oxides emission trends in East Asia observed from
607 space, Atmos. Chem. Phys., 13, 12003–12012, doi:10.5194/acp-13-12003-2013, 2013.
- 608 Miyazaki, K., Eskes, H. J., Sudo, K., Takigawa, M., van Weele, M., and Boersma, K. F.: Simultaneous assimilation
609 of satellite NO₂, O₃, CO, and HNO₃ data for the analysis of tropospheric chemical composition and emissions,
610 Atmos. Chem. Phys., 12, 9545– 9579, doi:10.5194/acp-12-9545-2012, 2012.
- 611 Miyazaki, K. and Eskes, H.: Constraints on surface NO_x emissions by assimilating satellite observations of multiple
612 species, Geophys. Res. Lett., 40, 4745–4750, doi:10.1002/grl.50894, 2013.
- 613 Miyazaki, K., Eskes, H. J., Sudo, K., and Zhang, C.: Global lightning NO_x production estimated by an assimilation
614 of multiple satellite data sets, Atmos. Chem. Phys., 14, 3277–3305, doi:10.5194/acp-14-3277-2014, 2014.
- 615 Mlawer, E. J., Taubman, S. J., Brown, P. D., Iacono, M. J., and Clough, S. A.: Radiative transfer for inhomogeneous
616 atmospheres: RRTM, a validated correlated-k model for the longwave, J. Geophys. Res.-Atmos., 102, 16663–
617 16682, doi:10.1029/97jd00237, 1997.
- 618 Nie, W., Ding, A., Wang, T., Kerminen, V.-M., George, C., Xue, L., Wang, W., Zhang, Q., Petäjä T., Qi, X., Gao,
619 X., Wang, X., Yang, X., Fu, C., and Kulmala, M.: Polluted dust promotes new particle formation and growth,
620 Sci. Rept., 4, 6634, 2014.
- 621 Pagowski, M., Grell, G. A., McKeen, S. A., Peckham, S. E., and Devenyi, D.: Three-dimensional variational data
622 assimilation of ozone and fine particulate matter observations: some results using the Weather Research and
623 Forecasting – Chemistry model and Grid-point Statistical Interpolation, Q. J. Roy. Meteor. Soc., 136, 2013–
624 2024, doi:10.1002/qj.700, 2010.
- 625 Pagowski, M., and Grell, G. A.: Experiments with the assimilation of fine aerosols using an ensemble Kalman filter,
626 J. Geophys. Res.-Atmos., 117, D21302, doi:10.1029/2012jd018333, 2012.
- 627 Pagowski, M., Liu, Z., Grell, G. A., Hu, M., Lin, H.-C., and Schwartz, C. S.: Implementation of aerosol assimilation
628 in Gridpoint Statistical Interpolation (v. 3.2) and WRF-Chem (v.3.4.1), Geosci. Model Dev., 7, 1621-1627,
629 <https://doi.org/10.5194/gmd-7-1621-2014>, 2014.
- 630 Parrish, D. D., M. Trainer, M. P. Buhr, B. A. Watkins, and F. C. Fehsenfeld, Carbon monoxide concentrations and
631 their relation to concentrations of total reactive oxidized nitrogen at two rural U.S. sites, J. Geophys. Res., 96,
632 9309– 9320, 1991.



- 633 Parrish, D. D., and Zhu, T.: Clean Air for Megacities, *Science*, 326, 674-675, 408 doi:10.1126/science.1176064,
634 2009.
- 635 Peng, Z., Zhang, M., Kou, X., Tian, X., and Ma, X.: A regional carbon data assimilation system and its preliminary
636 evaluation in East Asia, *Atmos. Chem. Phys.*, 15, 1087-1104, doi:10.5194/acp-15-1087-2015, 2015.
- 637 Peng, Z., Liu, Z., Chen, D., and Ban, J.: Improving PM_{2.5} forecast over China by the joint adjustment of initial
638 conditions and source emissions with an ensemble Kalman filter, *Atmos. Chem. Phys.*, 17, 4837-4855,
639 <https://doi.org/10.5194/acp-17-4837-2017>, 2017.
- 640 Pope, C. A.: Review: Epidemiological basis for particulate air pollution health standards, *Aerosol Sci. Tech.*, 32, 4–
641 14, 2000.
- 642 Pope, C. A., Burnett, R. T., Thun, M. J., Calle, E. E., Krewski, D., Ito, K., and Thurston, G. D.: Lung cancer,
643 cardiopulmonary mortality, and long-term exposure to fine particulate air pollution, *J. Am. Med. Assoc.*, 287,
644 1132–1141, 2002.
- 645 Sandu, A., Daescu, D., Carmichael, G. R., and Chai, T.: Adjoint sensitivity analysis of regional air quality models,
646 *J. Comput. Phys.*, 204, 222–252, 2005.
- 647 Schutgens, N. A. J., Miyoshi, T., Takemura, T., and Nakajima, T.: Sensitivity tests for an ensemble Kalman filter
648 for aerosol assimilation, *Atmos. Chem. Phys.*, 10, 6583–6600, doi:10.5194/acp-10-6583-2010, 2010a.
- 649 Schutgens, N. A. J., Miyoshi, T., Takemura, T., and Nakajima, T.: Applying an ensemble Kalman filter to the
650 assimilation of AERONET observations in a global aerosol transport model, *Atmos. Chem. Phys.*, 10, 2561–
651 2576, doi:10.5194/acp-10-2561-2010, 2010b.
- 652 Schutgens, N., Nakata, M., and Nakajima, T.: Estimating Aerosol Emissions by Assimilating Remote Sensing
653 Observations into a Global Transport Model, *Remote Sens.*, 4, 3528–3543, 2012.
- 654 Schwartz, C. S., Liu, Z., Lin, H. C., and McKeen, S. A.: Simultaneous three-dimensional variational assimilation of
655 surface fine particulate matter and MODIS aerosol optical depth, *J. Geophys. Res.*, 117, D13202,
656 doi:10.1029/2011JD017383, 2012.
- 657 Schwartz, C. S., Liu, Z., Lin, H.-C., and Cetola, J. D.: Assimilating aerosol observations with a “hybrid” variational-
658 ensemble data assimilation system, *J. Geophys. Res.-Atmos.*, 119, 4043–4069, doi:10.1002/2013JD020937,
659 2013.
- 660 Sekiyama, T. T., Tanaka, T. Y., Shimizu, A., and Miyoshi, T.: Data assimilation of CALIPSO aerosol observations,
661 *Atmos. Chem. Phys.*, 10, 39-49, doi:10.5194/acp-10-39-2010, 2010.
- 662 Stockwell, W. R., Kirchner, F., Kuhn, M., and Seefeld, S: A new mechanism for regional atmospheric chemistry
663 modeling, *J. Geophys. Res.*, 102(D22), 25,847–25,879, doi:10.1029/97JD00849, 1997.
- 664 Sun, Y. L., Wang, Z. F., Du, W., Zhang, Q., Wang, Q. Q., Fu, P. Q., Pan, X. L., Li, J., Jayne, J., and Worsnop, D.
665 R.: Longterm real-time measurements of aerosol particle composition in Beijing, China: seasonal variations,
666 meteorological effects, and source analysis, *Atmos. Chem. Phys.*, 15, 10149 - 10165, doi:10.5194/acp-15-
667 10149-2015, 2015.
- 668 Tang, X., Wang, Z. F., Zhu, J., Gbaguidi, A., Wu, Q. Z., Li, J., and Zhu, T.: Sensitivity of ozone to precursor
669 emissions in urban Beijing with a Monte Carlo scheme, *Atmos. Environ.*, 44, 3833–3842, 2010.
- 670 Tang, X., Zhu, J., Wang, Z. F., and Gbaguidi, A.: Improvement of ozone forecast over Beijing based on ensemble
671 Kalman filter with simultaneous adjustment of initial conditions and emissions, *Atmos. Chem. Phys.*, 11,
672 12901–12916, doi:10.5194/acp-11-12901-2011, 2011.
- 673 Tang, X., Zhu, J., Wang, Z. F., Wang, M., Gbaguidi, A., Li, J., Shao, M., Tang, G. Q., and Ji, D. S.: Inversion of CO
674 emissions over Beijing and its surrounding areas with ensemble Kalman filter, *Atmos. Environ.*, 81, 676–686,
675 2013.
- 676 Tang, X., Zhu, J., Wang, Z., Gbaguidi, A., Lin, C., Xin, J., Song, T., and Hu, B.: Limitations of ozone data



- 677 assimilation with adjustment of NO_x emissions: mixed effects on NO₂ forecasts over Beijing and surrounding
678 areas, *Atmos. Chem. Phys.*, 16, 6395–6405, <https://doi.org/10.5194/acp-16-6395-2016>, 2016.
- 679 van der A, R. J., Peters, D. H. M. U., Eskes, H., Boersma, K. F., Van Roozendaal, M., De Smedt, I., and Kelder, H.
680 M.: Detection of the trend and seasonal variation in tropospheric NO₂ over China, *J. Geophys. Res.*, 111,
681 D12317, doi:10.1029/2005JD006594, 2006.
- 682 van der A, R. J., Mijling, B., Ding, J., Koukouli, M. E., Liu, F., Li, Q., Mao, H., and Theys, N.: Cleaning up the air:
683 effectiveness of air quality policy for SO₂ and NO_x emissions in China, *Atmos. Chem. Phys.*, 17, 1775–1789,
684 <https://doi.org/10.5194/acp-17-1775-2017>, 2017.
- 685 van Loon, M., Builtjes, P. J. H., and Segers, A. J.: Data assimilation of ozone in the atmospheric transport chemistry
686 model LOTOS, *Environ. Model. Softw.*, 15, 603–609, 2000.
- 687 Wang, Z., Li, J., Wang, Z., Yang, W., Tang, X., Ge, B., Yan, P., Zhu, L., Chen, X., and Chen, H.: Modeling study
688 of regional severe hazes over mid-eastern China in January 2013 and its implications on pollution prevention
689 and control, *Sci.China-Earth Sci.*, 57, 3–13, 2014.
- 690 Whitaker, J. S., and Hamill, T. M.: Ensemble data assimilation without perturbed observations, *Mon. Weather Rev.*,
691 130, 1913–1924, 2002.
- 692 Wild, O., Zhu, X., and Prather, M. J.: Fast-j: Accurate simulation of in- and below-cloud photolysis in tropospheric
693 chemical models, *J. Atmos. Chem.*, 37, 245–282, doi:10.1023/A:1006415919030, 2000.
- 694 Xie, Y., Ding, A., Nie, W., Mao, H., Qi, X., Huang, X., Xu, Z., Kerminen, V.-M., Petäjä T., Chi, X., Virkkula, A.,
695 Boy, M., Xue, L., Guo, J., Sun, J., Yang, X., Kulmala, M., and Fu, C.: Enhanced sulfate formation by nitrogen
696 dioxide: Implications from in situ observations at the SORPES station, *J. Geophys. Res. – Atmos.*, 120, 24,
697 12679–12694, 2015.
- 698 Yang, Y. R., Liu, X. G., Qu, Y., An, J. L., Jiang, R., Zhang, Y. H., Sun, Y. L., Wu, Z. J., Zhang, F., Xu, W. Q., and
699 Ma, Q. X.: Characteristics and formation mechanism of continuous hazes in China: a case study during the
700 autumn of 2014 in the North China Plain, *Atmos. Chem. Phys.*, 15, 8165 – 8178, doi:10.5194/acp-15-8165-
701 2015, 2015.
- 702 Yumimoto, K., Uno, I., Sugimoto, N., Shimizu, A., Liu, Z., and Winker, D. M.: Adjoint inversion modeling of Asian
703 dust emission using lidar observations, *Atmos. Chem. Phys.*, 8, 2869–2884, doi:10.5194/acp-8-2869-2008, 2008.
- 704 Yumimoto, K., Uno, I., Sugimoto, N., Shimizu, A., and Satake, S.: Adjoint inverse modeling of dust emission and
705 transport over East Asia, *Geophys. Res. Lett.*, 34, L00806, doi:10.029/2006GL028551, 2007.
- 706 Zhang, Q., Streets, D. G., Carmichael, G. R., He, K. B., Huo, H., Kannari, A., Klimont, Z., Park, I. S., Reddy, S.,
707 Fu, J. S., Chen, D., Duan, L., Lei, Y., Wang, L. T., and Yao, Z. L.: Asian emissions in 2006 for the NASA
708 INTEX-B mission, *Atmos. Chem. Phys.*, 9, 5131–5153, doi:10.5194/acp-9-5131-2009, 2009.
- 709 Zhang, R., Wang, G., Guo, S., Zamora, M. L., Ying, Q., Lin, Y., Wang, W., Hu, M., and Wang, Y.: Formation of
710 Urban Fine Particulate Matter, *Chem. Rev.*, 115, 3803–3855, doi:10.1021/acs.chemrev.5b00067, 2015a.
- 711 Zhang, L., Shao, J. Y., Lu, X., Zhao, Y. H., Hu, Y. Y., Henze, D. K., et al.: Sources and processes affecting fine
712 particulate matter pollution over North China: An adjoint analysis of the Beijing APEC period. *Environmental
713 Science & Technology*, 50(16), 8731–8740. <https://doi.org/10.1021/acs.est.6b03010>, 2016.
- 714 Zhang, L., Li, Q., Wang, T., Ahmadov, R., Zhang, Q., Li, M., and Lv, M.: Combined impacts of nitrous acid and
715 nitryl chloride on lower-tropospheric ozone: new module development in WRF-Chem and application to China,
716 *Atmos. Chem. Phys.*, 17, 9733–9750, <https://doi.org/10.5194/acp-17-9733-2017>, 2017.
- 717 Zhao, X. J., Zhao, P. S., Xu, J., Meng, W., Pu, W. W., Dong, F., He, D., and Shi, Q. F.: Analysis of a winter regional
718 haze event and its formation mechanism in the North China Plain, *Atmos. Chem. Phys.*, 13, 5685 – 5696,
719 doi:10.5194/acp-13-5685-2013, 2013.
- 720 Zheng, B., Zhang, Q., Zhang, Y., He, K. B., Wang, K., Zheng, G. J., Duan, F. K., Ma,



721 Y. L., and Kimoto, T.: Heterogeneous chemistry: a mechanism missing in current models
722 to explain secondary inorganic aerosol formation during the January 2013 haze episode in North
723 China, Atmos.Chem.Phys., 15, 2031-2049, 10.5194/acp-15-2031-2015, 2015.

724

725 **List of Figures and Tables**

726 Table 1. WRF-Chem model configurations in this study.

727 Table 2. State vectors in the data assimilation system.

728 Figure 1. The model domain (left) and the North China Plain (right). Black dots are the
729 observational sites used for assimilation, and red stars are the observational sites used
730 for validation. The green frame marks the Beijing–Tianjin–Hebei region.

731 Figure 2. Time series of prior ensemble mean RMSE (blue line) and total spread (black
732 line) for PM_{2.5}, PM₁₀, SO₂, NO₂, CO and O₃ concentrations aggregated over all
733 observations over the Beijing–Tianjin–Hebei region. Units for all these variables are
734 $\mu\text{g m}^{-3}$.

735 Figure 3. Time series of the area-averaged ensemble spread for the emission scaling
736 factors over the Beijing–Tianjin–Hebei region.

737 Figure 4. Time series of the hourly pollutant concentrations in the Beijing–Tianjin–
738 Hebei (BTH) region obtained from observations (red line), the control run (black line),
739 the analysis (pink line), the first-day forecast from fcICsEs (fcICsEs24, blue line), and
740 the first-day forecast from fcICs (fcICs24, blue line). The observations were obtained
741 from the 47 independent sites in the BTH region. The modelled time series were
742 interpolated to the 47 independent sites using the spatial bilinear interpolator method.
743 The shaded backgrounds indicate the distribution of the observations, where the top
744 edge represented the 90th percentile and the bottom edge the 10th percentile. Units:
745 $\mu\text{g m}^{-3}$.

746 Table 3. Comparison with observations of the surface PM_{2.5} mass concentrations in the
747 Beijing–Tianjin–Hebei region from the control experiment, the assimilation experiment,
748 and the first-day forecast, over all analysis times from 6 to 16 October 2014. Units:
749 $\mu\text{g m}^{-3}$.

750 Figure 5. Bias of surface PM_{2.5}, PM₁₀, SO₂, NO₂, CO and O₃ as a function of forecast
751 range calculated against all the independent observations over the Beijing–Tianjin–
752 Hebei region shown in Figure 1. The 72-h forecasts were performed at each 0000 UTC
753 from 6 to 14 October 2014 and the statistics were computed from 6 to 14 October. Units:
754 $\mu\text{g m}^{-3}$.



755 Figure 6. As in Figure 5 but for RMSE. Units: $\mu\text{g m}^{-3}$.

756 Figure 7. Normalized RMSE (assimilation divided by control) for fcICsEs and fcICs
757 for $\text{PM}_{2.5}$, PM_{10} , SO_2 and CO.

758 Figure 8. Spatial distribution of the prescribed emissions (top panels) of $\text{PM}_{2.5}$ (left), PM_{10} (middle),
759 and NH_3 (right) and the corresponding time-averaged differences between the ensemble mean
760 analysis and the prescribed values at the lowest model level averaged over all hours from 6 to
761 16 October 2014 in the NCP region. Units for $\text{PM}_{2.5}$ and PM_{10} emissions: $\mu\text{g}\cdot\text{m}^{-2}\cdot\text{s}^{-1}$; and
762 for NH_3 emissions: $\text{mol}\cdot\text{km}^{-2}\cdot\text{hr}^{-1}$.

763 Figure 9. As in Figure 8 but for SO_2 (left), NO (middle), and CO (right). Units for SO_2 , NO
764 and CO emissions: $\text{mol}\cdot\text{km}^{-2}\cdot\text{hr}^{-1}$.

765 Figure 10. Hourly area-averaged time series extracted from the analyzed emission
766 scaling factors (black line), the forecast emission scaling factors (green dashed line),
767 the analyzed emissions (blue line), and the prescribed emissions (blue dashed line) in
768 the Beijing–Tianjin–Hebei region. Units for $\text{PM}_{2.5}$ and PM_{10} emissions: $\mu\text{g}\cdot\text{m}^{-2}\cdot\text{s}^{-1}$; and
769 for NH_3 , SO_2 , NO and CO emissions: $\text{mol}\cdot\text{km}^{-2}\cdot\text{hr}^{-1}$.
770



771

772

Table 1. WRF-Chem model configurations in this study.

Parameterization	WRF-Chem Option
Aerosol scheme	Goddard Chemistry Aerosol Radiation and Transport (Chin et al., 2000, 2002)
Photolysis scheme	Fast-J (Wild et al., 2000)
Gas-phase chemistry	Regional Atmospheric Chemistry Mechanism (Stockwell et al., 1997)
Microphysics	the WRF single-moment 5 class scheme
Longwave radiation	Rapid Radiative Transfer Model longwave scheme (Mlawer et al., 1997)
shortwave radiation	Goddard shortwave radiation scheme (Chou and Suarez, 1994)
Planetary boundary layer	Yonsei University boundary layer scheme (Hong et al., 2006)
cumulus parameterization	Grell-3D scheme
Land-surface model	NOAH (Chen and Dudhia, 2001)
Dust and sea salt emissions	Goddard Chemistry Aerosol Radiation and Transport (Chin et al., 2002)

773

774



775

776

Table 2. State vectors in the data assimilation system.

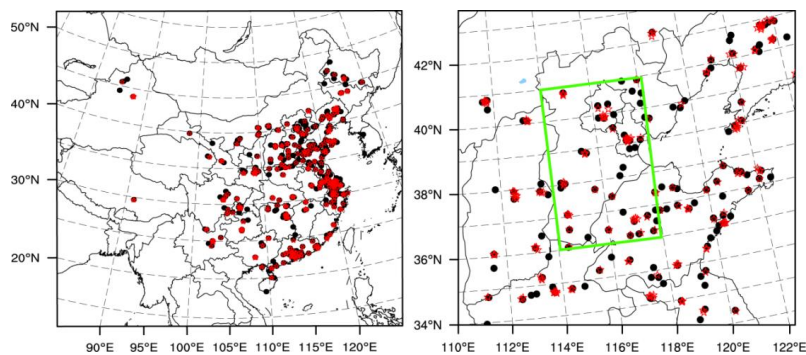
Observations	PM _{2.5}	PM _{10-2.5}	SO ₂	NO ₂	CO	O ₃
Mass	P ₂₅ , S, OC ₁ , OC ₂	BC ₁ , P ₁₀ , D ₃ , D ₄ ,		NO,		
concentration	BC ₂ , D ₁ , D ₂ , S ₁ , S ₂	D ₅ S ₃ , S ₄ ,	SO ₂	NO ₂	CO	O ₃
Scaling factors	$\lambda_{\text{PM}_{2.5}}$, λ_{NH_3}	$\lambda_{\text{PM}_{10}}$	λ_{SO_2}	λ_{NO}	λ_{CO}	—

777

778



779

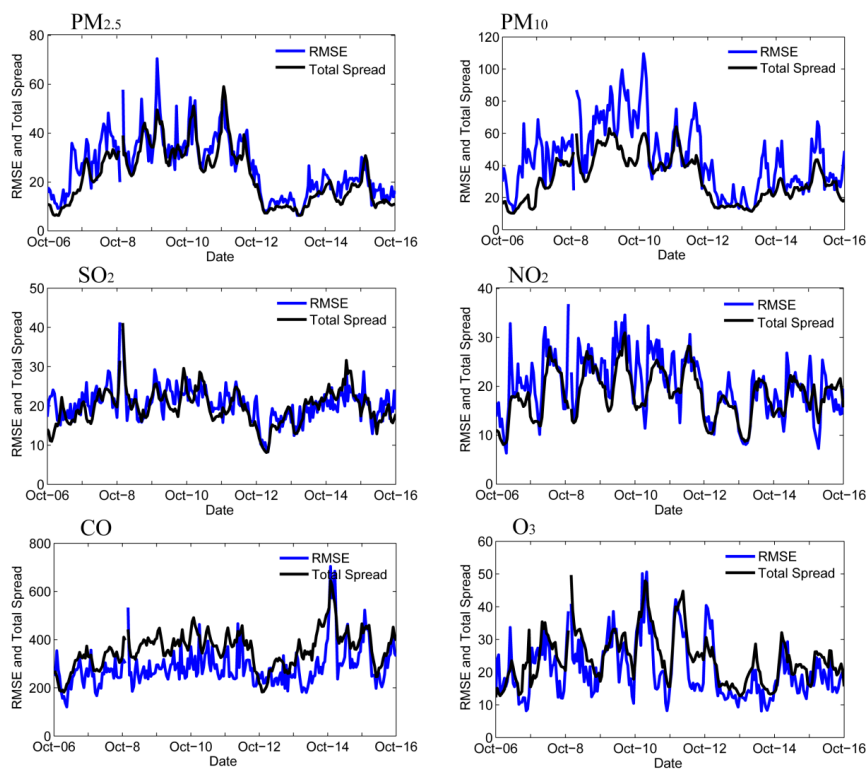


780

781 Figure 1. The model domain (left) and the North China Plain (right). Black dots are
782 the observational sites used for assimilation, and red stars are the observational sites
783 used for validation. The green frame marks the Beijing–Tianjin–Hebei region.
784



785



786

787

788 Figure 2. Time series of prior ensemble mean RMSE (blue line) and total spread

789 (black line) for PM_{2.5}, PM₁₀, SO₂, NO₂, CO and O₃ concentrations aggregated over all

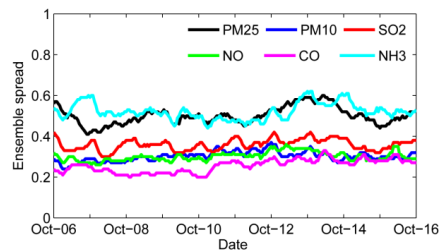
790 observations over the Beijing–Tianjin–Hebei region. Units for all these variables are

791 $\mu\text{g m}^{-3}$.



792

793



794

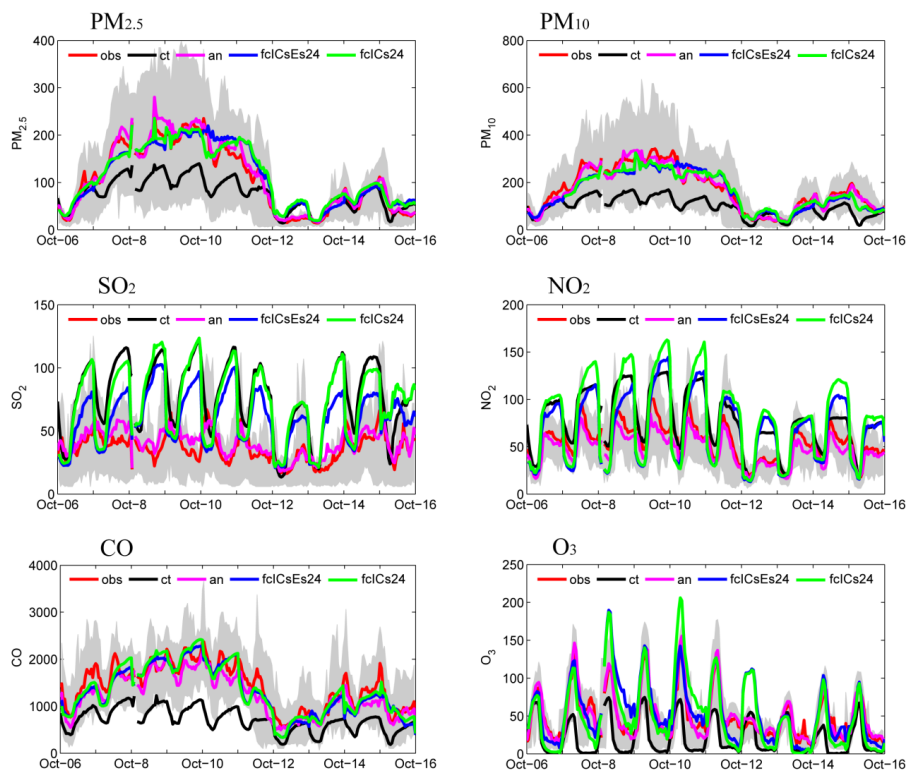
795 Figure 3. Time series of the area-averaged ensemble spread for the emission scaling

796 factors over the Beijing–Tianjin–Hebei region.

797



798



799

800

801

802

803

804

805

806

807

808

809

810

Figure 4. Time series of the hourly pollutant concentrations in the Beijing–Tianjin–Hebei (BTH) region obtained from observations (red line), the control run (black line), the analysis (pink line), the first-day forecast from fclCsEs (fclCsEs24, blue line), and the first-day forecast from fclCs (fclCs24, blue line). The observations were obtained from the 47 independent sites in the BTH region. The modelled time series were interpolated to the 47 independent sites using the spatial bilinear interpolator method. The shaded backgrounds indicate the distribution of the observations, where the top edge represented the 90th percentile and the bottom edge the 10th percentile.

Units: $\mu\text{g m}^{-3}$.

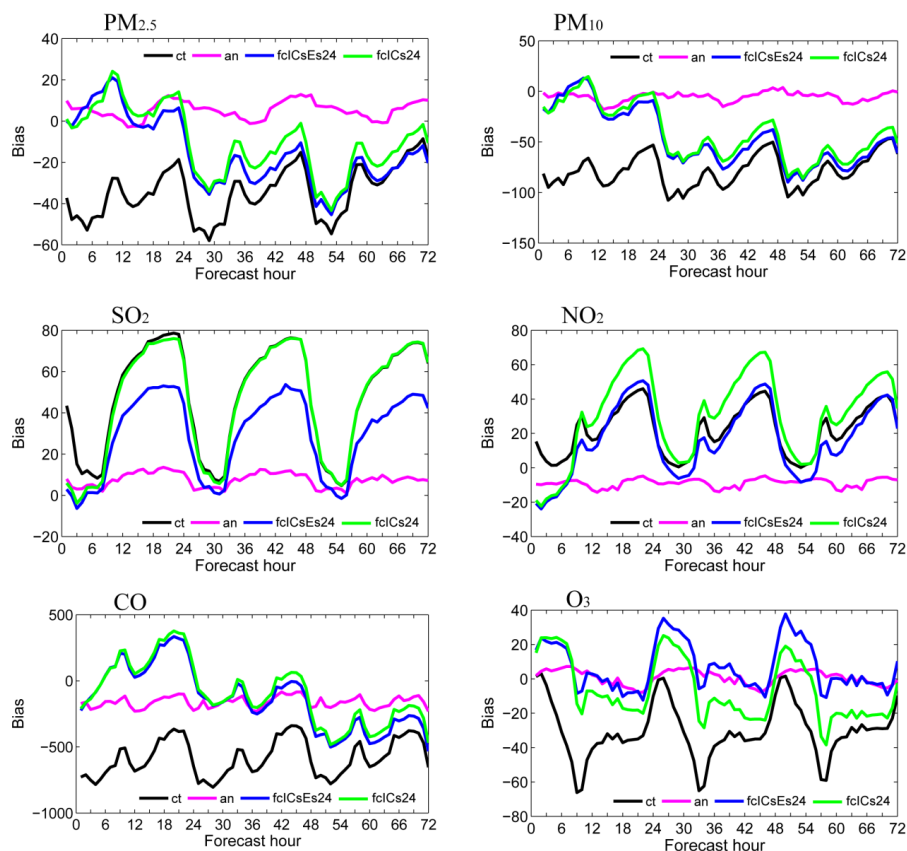


811 Table 3. Comparison with observations of the surface PM_{2.5} mass concentrations in the Beijing–
 812 Tianjin–Hebei region from the control experiment, the assimilation experiment, and the first-day
 813 forecast, over all analysis times from 6 to 16 October 2014. Units: $\mu\text{g m}^{-3}$.

Species	Experiment	Mean observed	Mean simulated	BIAS	RMSE	CORR
		value	value			
PM _{2.5}	Control		80.7	−34.1	92.1	0.740
	Analysis	114.8	119.9	5.1	51.5	0.891
	fcICsEs24		121.2	6.5	77.8	0.736
	fcICs24		123.1	8.3	75.1	0.748
PM ₁₀	Control		96.9	−77.7	134.6	0.691
	Analysis	174.6	169.0	−5.6	63.4	0.890
	fcICsEs24		162.7	−11.9	98.7	0.716
	fcICs24		164.3	−10.3	95.9	0.726
SO ₂	Control		81.1	48.1	66.6	0.088
	Analysis	33.0	41.1	8.1	27.9	0.540
	fcICsEs24		62.0	29.0	51.2	0.120
	fcICs24		75.7	42.7	65.8	0.038
NO ₂	Control		78.8	22.4	39.7	0.545
	Analysis	56.4	48.0	−8.3	31.7	0.557
	fcICsEs24		71.8	15.4	46.2	0.408
	fcICs24		82.8	26.4	55.5	0.414
CO	Control		752.3	−565.7	962.7	0.354
	Analysis	1318.0	1157.5	−160.4	618.9	0.705
	fcICsEs24		1418.4	100.4	805.1	0.476
	fcICs24		1448.2	130.2	838.2	0.439
O ₃	Control		26.5	−31.0	50.8	0.463
	Analysis	57.5	59.6	2.1	31.1	0.753
	fcICsEs24		63.5	6.0	49.0	0.460
	fcICs24		58.98	1.5	50.5	0.478

814

815



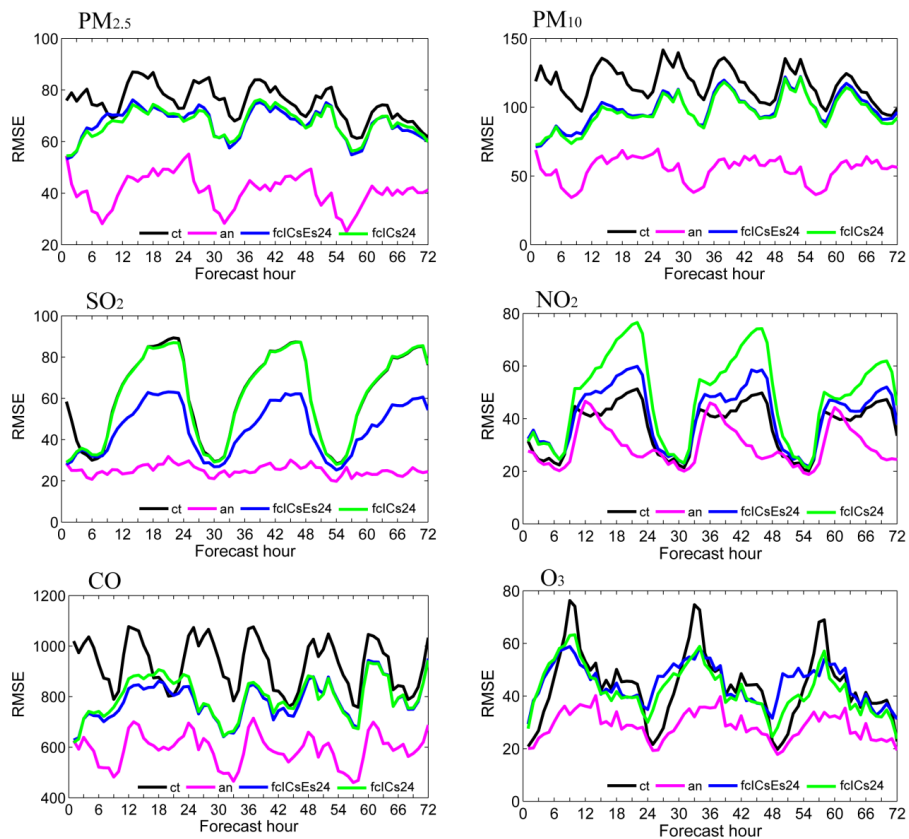
816

817 Figure 5. Bias of surface PM_{2.5}, PM₁₀, SO₂, NO₂, CO and O₃ as a function of forecast
818 range calculated against all the independent observations over the Beijing–Tianjin–
819 Hebei region shown in Figure 1. The 72-h forecasts were performed at each 0000
820 UTC from 6 to 14 October 2014 and the statistics were computed from 6 to 14
821 October. Units: $\mu\text{g m}^{-3}$.

822



823



824

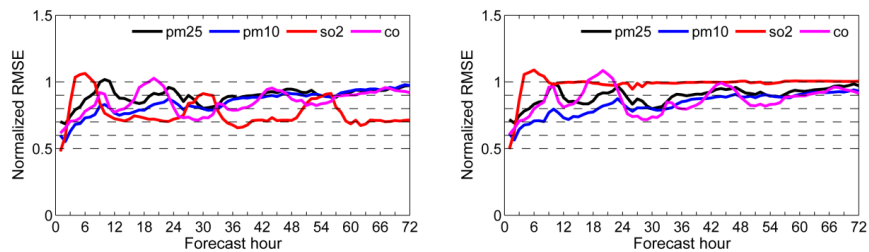
825

826

Figure 6. As in Figure 5 but for RMSE. Units: $\mu\text{g m}^{-3}$.



827



828

829

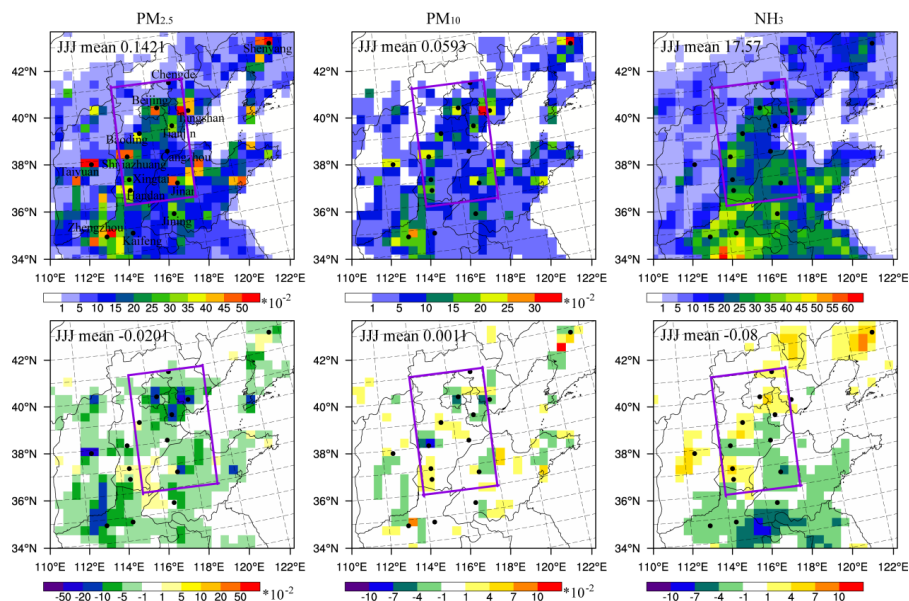
830

831

Figure 7. Normalized RMSE (assimilation divided by control) for fcICsEs and fcICs for PM_{2.5}, PM₁₀, SO₂ and CO.



832



833

834

Figure 8. Spatial distribution of the prescribed emissions (top panels) of PM_{2.5} (left), PM₁₀

835

(middle), and NH₃ (right) and the corresponding time-averaged differences between the ensemble

836

mean analysis and the prescribed values at the lowest model level averaged over all hours

837

from 6 to 16 October 2014 in the NCP region. Units for PM_{2.5} and PM₁₀ emissions:

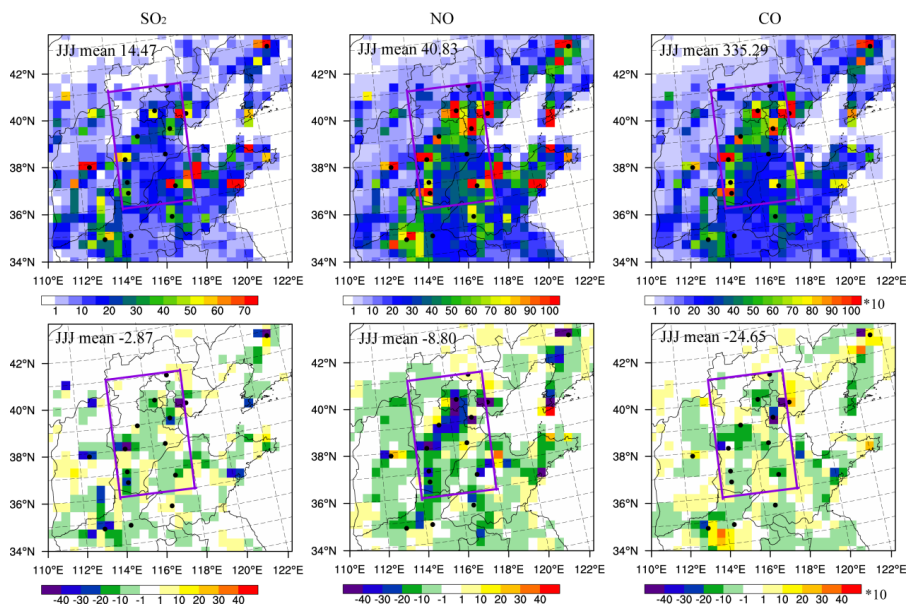
838

$\mu\text{g}\cdot\text{m}^{-2}\cdot\text{s}^{-1}$; and for NH₃ emissions: $\text{mol}\cdot\text{km}^{-2}\cdot\text{hr}^{-1}$.

839



840



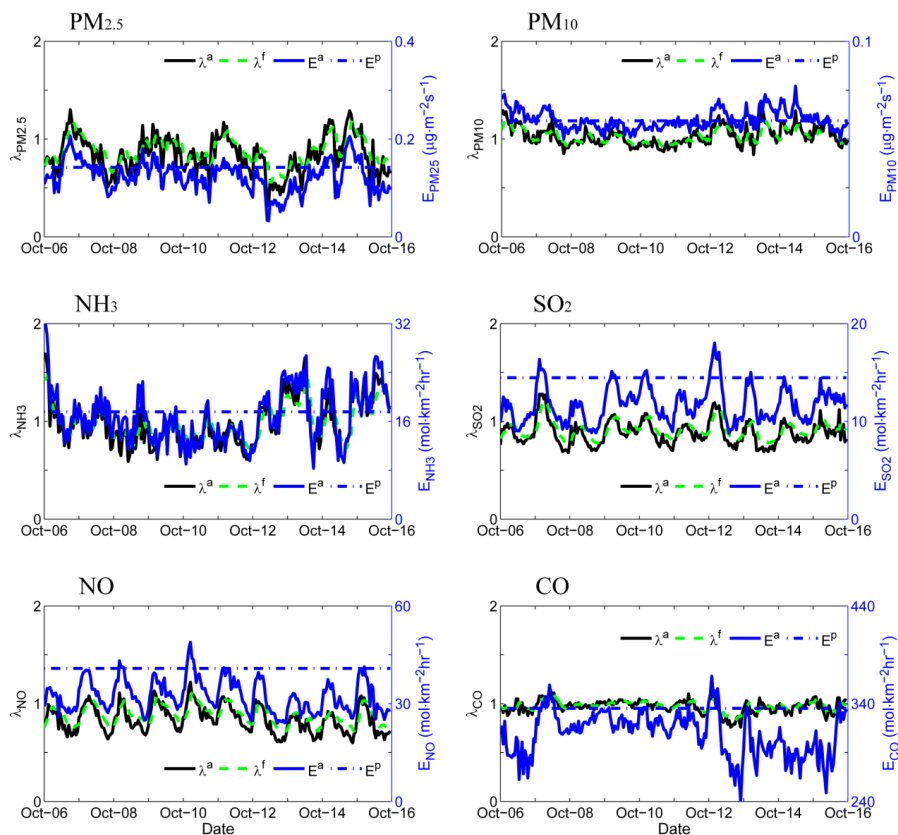
841

842 Figure 9. As in Figure 8 but for SO₂ (left), NO (middle), and CO (right). Units for SO₂, NO
843 and CO emissions: mol·km⁻²·hr⁻¹.

844



845



846

847

848 Figure 10. Hourly area-averaged time series extracted from the analyzed emission

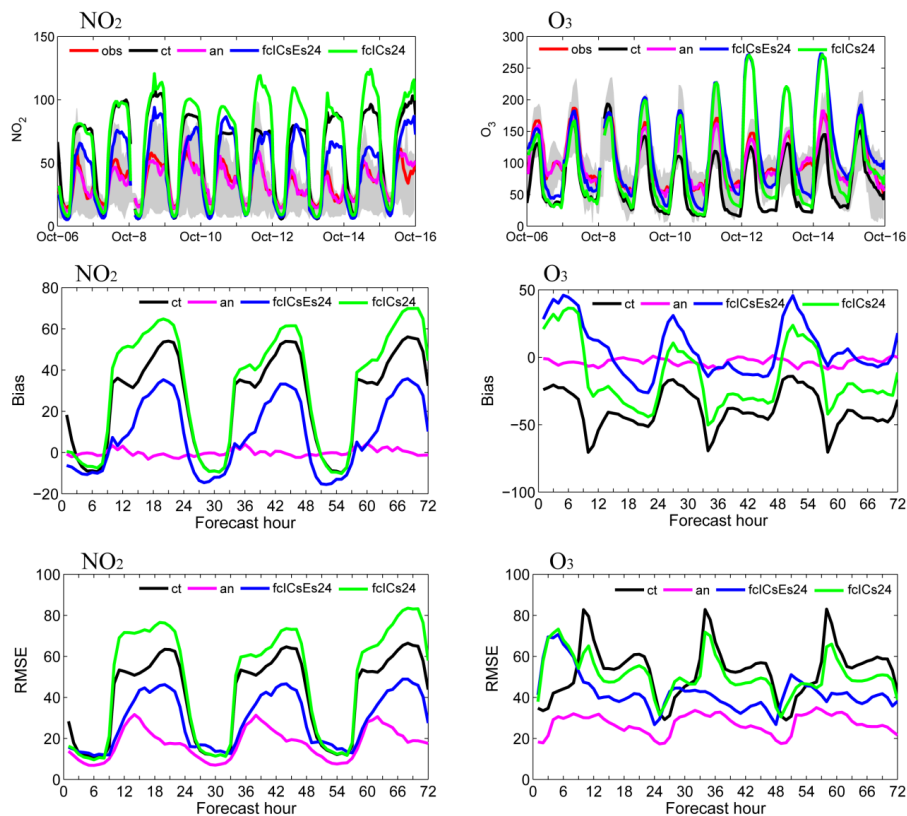
849 scaling factors (black line), the forecast emission scaling factors (green dashed line),

850 the analyzed emissions (blue line), and the prescribed emissions (blue dashed line)

851 in the Beijing-Tianjin-Hebei region. Units for PM_{2.5} and PM₁₀ emissions: $\mu\text{g}\cdot\text{m}^{-2}\cdot\text{s}^{-1}$;852 and for NH₃, SO₂, NO and CO emissions: $\text{mol}\cdot\text{km}^{-2}\cdot\text{hr}^{-1}$.



853



854

855 Figure 11. NO_2 and O_3 time series of the hourly pollutant concentrations in the Pearl
 856 River Delta region (PRD, $21^\circ\text{--}24^\circ\text{N}$, $112.5^\circ\text{--}115^\circ\text{E}$) obtained from observations (red
 857 line), the control run (black line), the analysis (pink line), the first-day forecast from
 858 fclCsEs (fclCsEs24, blue line), and the first-day forecast from fclCs (fclCs24, blue
 859 line). The bias and RMSEs of surface NO_2 and O_3 as a function of forecast range
 860 calculated against all the independent observations (34 sites) over the PRD region.

861

Units: $\mu\text{g m}^{-3}$.